












## Characterization of an imploding cylindrical plasma for electron transport studies using x-ray emission spectroscopy

Cite as: Phys. Plasmas **27**, 023302 (2020); <https://doi.org/10.1063/1.5125271>

Submitted: 22 August 2019 . Accepted: 07 January 2020 . Published Online: 04 February 2020

M. Dozières , S. Hansen, P. Forestier-Colleoni, C. McGuffey , D. Kawahito, M. Bailly-Grandvaux, K. Bhutwala, C. M. Krauland, M. S. Wei , P. Gourdain , J. R. Davies , K. Matsuo , S. Fujioka , E. M. Campbell , J. L. Peebles , J. J. Santos , D. Batani, S. Zhang , and F. N. Beg



View Online



Export Citation



CrossMark

### ARTICLES YOU MAY BE INTERESTED IN

[Experimental study of hot electron generation in shock ignition relevant high-intensity regime with large scale hot plasmas](#)

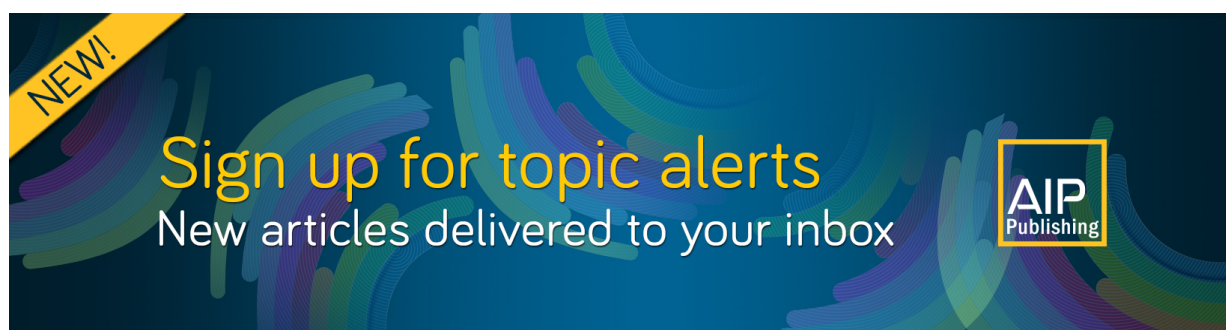
Phys. Plasmas **27**, 023111 (2020); <https://doi.org/10.1063/1.5119250>

[Extended-magnetohydrodynamics in under-dense plasmas](#)

Phys. Plasmas **27**, 022103 (2020); <https://doi.org/10.1063/1.5124144>

[Development of a directly driven multi-shell platform: Laser drive energetics](#)

Phys. Plasmas **27**, 022706 (2020); <https://doi.org/10.1063/1.5100518>



# Characterization of an imploding cylindrical plasma for electron transport studies using x-ray emission spectroscopy

Cite as: Phys. Plasmas **27**, 023302 (2020); doi: [10.1063/1.5125271](https://doi.org/10.1063/1.5125271)

Submitted: 22 August 2019 · Accepted: 7 January 2020 ·

Published Online: 4 February 2020



View Online



Export Citation



CrossMark

M. Dozières,<sup>1,a)</sup> S. Hansen,<sup>2</sup> P. Forestier-Colleoni,<sup>1</sup> C. McGuffey,<sup>1</sup> D. Kawahito,<sup>1</sup> M. Bailly-Grandvaux,<sup>1</sup> K. Bhutwala,<sup>1</sup> C. M. Krauland,<sup>3</sup> M. S. Wei,<sup>4</sup> P. Gourdain,<sup>4</sup> J. R. Davies,<sup>5</sup> K. Matsuo,<sup>6</sup> S. Fujioka,<sup>6</sup> E. M. Campbell,<sup>5</sup> J. L. Peebles,<sup>5</sup> J. J. Santos,<sup>7</sup> D. Batani,<sup>7</sup> S. Zhang,<sup>1</sup> and F. N. Beg<sup>1</sup>

## AFFILIATIONS

<sup>1</sup>Center for Energy Research, University of California, San Diego, La Jolla, California 92093-0417, USA

<sup>2</sup>Sandia National Laboratories, Albuquerque, New Mexico 87185, USA

<sup>3</sup>General Atomics, San Diego, California 92186, USA

<sup>4</sup>Extreme State Physics Laboratory, Physics and Astronomy Department, University of Rochester, Rochester, New York 14627, USA

<sup>5</sup>Laboratory for Laser Energetics, University of Rochester, Rochester, New York 14623, USA

<sup>6</sup>Institute of Laser Engineering, Osaka University, Suita, Osaka 565-0871, Japan

<sup>7</sup>Université de Bordeaux-CNRS-CEA, CELIA UMR 5107, F-33400 Talence, France

<sup>a)</sup>Author to whom correspondence should be addressed: [mdoziers@ucsd.edu](mailto:mdoziers@ucsd.edu)

## ABSTRACT

We report on the characterization of the conditions of an imploding cylindrical plasma by time-resolved x-ray emission spectroscopy. Knowledge about this implosion platform can be applied to studies of particle transport for inertial confinement fusion schemes or to astrophysical plasmas. A cylindrical Cl-doped CH foam within a tube of solid CH was irradiated by 36 beams ( $I_{\text{total}} \sim 5 \times 10^{14} \text{ W/cm}^2$ , 1.5 ns square pulse, and  $E_{\text{total}} \sim 16.2 \text{ kJ}$ ) of the OMEGA-60 laser to radially compress the CH toward the axis. The analysis of the time-resolved spectra showed that the compression can be described by four distinct phases, each presenting different plasma conditions. First the ablation of the cylinder is dominant; second, the foam is heated and induces a significant jump in emission intensities; third, the temperature and density of the foam reaches a maximum; and finally, the plasma expands. Ranges for the plasma temperature were inferred with the atomic physics code SCRAM (Spectroscopic Collisional-Radiative Atomic Model) and the experimental data have been compared to hydrodynamic simulations performed with the 2D code FLASH, which showed a similar implosion dynamic over time.

Published under license by AIP Publishing. <https://doi.org/10.1063/1.5125271>

## INTRODUCTION

Compressed plasmas are common in astrophysical environments<sup>1–3</sup> and High Energy Density Physics (HEDP) systems.<sup>4,5</sup> Understanding the behavior of matter undergoing compression can be complicated by hydrodynamic instabilities,<sup>6</sup> radiation transport,<sup>7</sup> and/or magnetic compression.<sup>8</sup> Such plasmas are mainly relevant for stellar core studies<sup>9,10</sup> and fusion schemes such as inertial confinement fusion (ICF)<sup>11,12</sup> and pulsed-power-driven cylindrical implosions.<sup>13,14</sup> One of the advanced ICF concepts is called fast ignition (FI). In this concept, ion,<sup>15</sup> proton,<sup>16</sup> or electron beams<sup>17</sup> are used to ignite a pre-compressed fuel. Isochoric beam heating of a pre-compressed target could create extreme high-energy-density states like those required to trigger ignition

for high-gain ICF. A high-intensity short-pulse laser ( $\geq 10^{20} \text{ W/cm}^2$  and  $\sim 10 \text{ ps}$ ) can be an efficient source of the required relativistic electron beams or energetic ions.<sup>18,19</sup> Relativistic electron transport through warm dense matter and hot dense plasmas underlies many other applications, such as a secondary source of particles or photons<sup>20,21</sup> or heating of dense matter for validating atomic physics models.<sup>22,23</sup>

While intense electron beam transport has been explored in imploding targets at large laser facilities in the context of FI,<sup>24–26</sup> physical and technical barriers exist that limit the energy and number of relativistic electrons that can reach and effectively heat the core plasma. In the literature, one can find several experimental platforms to study relativistic electron transport such as Jarrott *et al.*,<sup>26</sup>

Perez *et al.*,<sup>27</sup> or Norreys *et al.*<sup>28</sup> to investigate these issues. Many of them agree that in order to understand the electron transport data, a full experimental characterization of the implosion of the target is necessary.

These needs led us to develop a platform to create and characterize a compressed volume and study the energy deposition of relativistic electrons in it with cylindrical geometry aligned to the intense laser axis. This simple platform provides a basic physics understanding of compressed matter and relativistic beam–plasma interaction<sup>29,30</sup> for fundamental interest and for FI. The platform is also compatible with an axial magnetic field, which may benefit FI and is an essential aspect of the Magnetized Liner Inertial Fusion (MagLIF) concept.<sup>13,31</sup>

We present in this paper a detailed temporally resolved characterization of the compression of a cylindrically imploded target designed specifically to be compatible with studies of relativistic electron transport. We show time resolved x-ray emission spectra illustrating the evolution of the imploding target and atomic physics calculations that allow the inference of the plasma temperature at a given time. Finally, we compare the experimental data to hydrodynamics simulations describing the plasma conditions over time.

## EXPERIMENTAL SETUP

The experiment was performed at the OMEGA-60 laser facility (Rochester, NY) and consisted of 36 beams (1.5 ns square pulse with rise times of  $\sim 0.1$  ns and  $\sim 450$  J per beam) irradiating a cylindrical target with a total intensity of  $\sim 5 \times 10^{14}$  W/cm<sup>2</sup>. The target was composed of a CH foam (0.1 g/cc) doped with 1% of Cl (by atom) within a tube of solid CH. CH foils of 10  $\mu$ m thickness were placed on each end of the cylinder in order to hold the foam in place during the compression. The cylinder was 600  $\mu$ m in outer diameter and 560  $\mu$ m in inner diameter. In order to protect the ends of the cylinder, each side was equipped with a shield cone made of solid CH with a density of 1 g/cm<sup>3</sup>. Figure 1 shows all the target details and a time-integrated x-ray

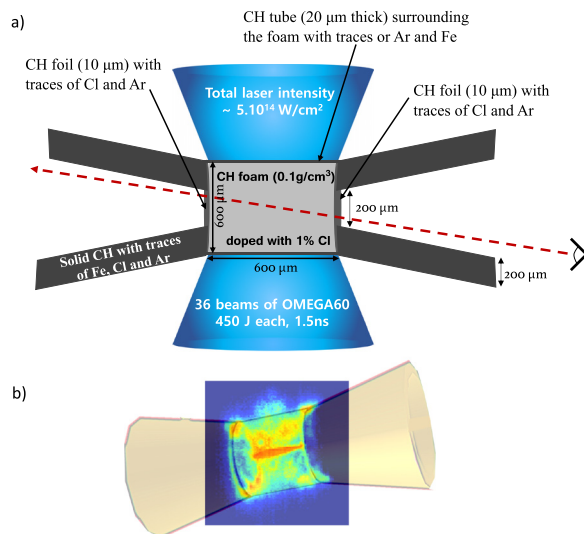


**FIG. 1.** (a) Experimental setup. (b) Example of the time-integrated x-ray pinhole image of the cylinder emission with 3D rendering overlaid of the target.

image with 3D rendering overlaid illustrating the size and the position of the cones in relation to the foam cylinder.

Each part of the target was tested under vacuum by x-ray fluorescence (XRF) in order to identify impurities. As noted in Fig. 1(a), Cl was detected not only in the foam but also in the cones. Traces of Fe were detected in the cones and the tube, and possible Ar contamination in all the parts of the target leads to a difficult energy calibration of the data. In future experiments, this contamination issue can be avoided by using a different Z material as a dopant in order to detect lines away from Ar and Fe K-shell spectral ranges. The dopant would also need to have relevant and analyzable spectra at the expected foam temperatures ( $\sim 300$ –600 eV).

The main diagnostic was a Streaked X-ray Spectrometer (SXS).<sup>32</sup> It consists of a flat RbAP crystal coupled to a streak camera equipped with a film as the detector. This setup provided time-resolved data over a detection window of 4 ns with a resolution of 2 ps per pixel. The spectral range was centered on Cl lines, from 2500 eV to 3500 eV. This spectrometer was placed towards the cylinder along its axis as illustrated by the red dotted arrow in Fig. 1(a). Considering the distance of the spectrometer from the target, even if the detection axis is towards the foam, the emission coming from any other part of the target can be detected. The entire setup provided spectra with a resolution  $E/\Delta E \sim 300$ .

In addition, four x-ray pinhole cameras with a spectral range from 2 keV to 5 keV observed the target emission at different angles in order to monitor the reproducibility of the shots. These diagnostics provided time integrated images with a magnification of 3.95, giving a resolution of 10  $\mu$ m per pixel as illustrated by the example in Fig. 1(b).

## X-RAY EMISSION SPECTRA

All the SXS data were corrected according to the film response, the filters used, and a calculated reflectivity of the crystal. The SXS spectra are displayed in Figs. 2 and 4–7 with equally scaled arbitrary units. Furthermore, the data are spectrally calibrated in energy with an error of  $\pm 30$  eV. The error of the spectral calibration is mainly due to the fact that the emission detected comes from different spatial positions.

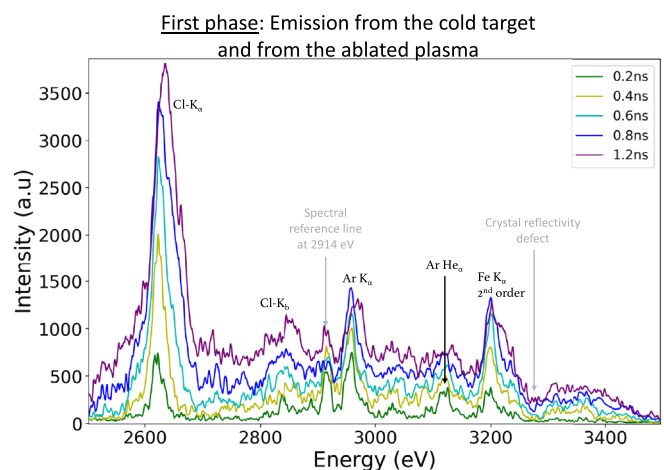


**FIG. 2.** X-ray emission spectra of the cylinder from 0.2 ns to 1.2 ns; each spectrum represents a different time. The line at  $\sim 2.9$  keV is artificial (created by a fiducial) and represents only a reference point for the spectral calibration.

The spectra presented correspond to the emission of the cylinder from  $t = 0$  ns, defined as 2% of the peak laser, to  $t = 2$  ns. Considering the jitter of the streak camera and the error defining the time zero for the images, the data are time-calibrated at  $\pm 120$  ps.

We detected emission coming from the cylinder over 2 ns, which consists of several emission lines from Cl, Ar, and Fe and a continuum emission smoothly increasing until 1.7 ns and then decaying. All the lines visible on the spectra are summarized in Table I.

As mentioned above, the target contains multiple elements in all its parts (cone, foam, and tube), all of which are detected by SXS. Because these parts have very different plasma conditions, a detailed, quantitative analysis of the emission lines was not possible. However, we were still able to extract information about the target conditions based on the evolution of the lines and bright continuum emission. From the emission, we distinguish four phases characterizing the heating and compression of the target.

First, during about a nanosecond, the laser-target interaction dominates, and we detect mainly narrow  $K_\alpha$  lines that we take to be due to hot-electron-generated fluorescence throughout the target and not from photoexcitation, with the temperature of the coronal plasma region ( $\sim 1.8$  keV) being too low to induce Cl  $K_\alpha$  emission (2.6 keV). Figure 2 shows the cylinder emission spectra from 0.2 ns to 1.2 ns where we can see Cl, Ar, and Fe 2nd order  $K_\alpha$  lines, as well as Cl  $K_\beta$  and Ar  $He_\alpha$  lines. At early times, only the external part of the cylinder is heated, while the center of the foam remains cold and at low density.

The Ar  $He_\alpha$  line most likely arises from the coronal plasma region where temperature is about 1.8 keV and constitutes the only part hot enough to create He-like Ar ions. Considering that the signal of the Ar  $He_\alpha$  line is only visible until about 1 ns, one can assume that past this time, the emission coming from the center of the foam dominates over that coming from the ablated plasma. During the same period, hot electrons are generated likely due to two-plasmon-decay and/or stimulated Raman scattering instabilities<sup>33–35</sup> and induce  $K_\alpha$  lines that are emitted from the cold part of the foam and from the cones located on each end of the cylinder. We stress that the quantity of hot electrons or their production was not the purpose of this study, so no further investigation has been done during this experiment. We can see a significant blue shift of the three  $K_\alpha$  lines in Fig. 2, indicating an increase in the temperature of the foam and the cones. The continuum rises slowly during this period, but past 1 ns, the Ar  $He_\alpha$  signal is overtaken by the continuum and cannot be further resolved. This observation is

TABLE I. Atomic transition details of all the lines visible in Figs. 2–5.

Label	Transition	Emitting ions	Theoretical energy (keV)
Cl $K_\alpha$	1s-2p	Cl <sup>1+</sup> -Cl <sup>6+</sup>	2.62
Cl $He_\alpha$	1s-2p	Cl <sup>15+</sup>	2.78
Cl $K_\beta$	1s-3p	Cl <sup>1+</sup> -Cl <sup>6+</sup>	2.81
Ar $K_\alpha$	1s-2p	Ar <sup>1+</sup> -Ar <sup>6+</sup>	2.96
Ar satellites	1s-2p	Ar <sup>9+</sup> -Ar <sup>13+</sup>	3.0–3.1
Ar $He_\alpha$	1s-2p	Ar <sup>16+</sup>	3.13
Fe $K_\alpha$ 2nd order	1s-2p	Fe <sup>1+</sup> -Fe <sup>6+</sup>	3.2
Cl $He_\beta$	1s-3p	Cl <sup>15+</sup>	3.27

consistent with emission from the heated and compressing foam becoming brighter than emission from the expanding ablating plasma.

We use the collisional-radiative code, SCRAM (Spectroscopic Collisional-Radiative Atomic Model),<sup>36</sup> to model spectra. SCRAM uses detailed atomic structure data from FAC (Flexible Atomic Code)<sup>37</sup> and geometry-dependent escape factors to account for optical depth effects. Fitting the observed  $K_\alpha$  line ratios of an early time spectrum gives the rough proportions of each element present in the target and refines the energy calibration of the spectrometer. Figure 3 shows a recorded spectrum compared to the experimental spectrum obtained at 0.4 ns. The yellow spectrum indicates proportions of 9000:6:3:1 for C, Cl, Ar, and Fe, respectively. Here, we neglect the line transport and spatial gradients and assume that all the observed fluorescence lines are driven by the same population of 20 keV hot electrons in cold target material and ambient density.

These proportions are consistent with the XRF characterization of the target, which indicated mainly Cl with traces of Fe and Ar. As both the foam and enclosing cylinder were composed of CH, carbon represents the most abundant element (the contribution of H is insignificant on the spectral range detected here).

In the second phase of the compression, Ar satellite lines begin to emerge from the continuum after 1.3 ns, as shown in Fig. 4, which indicates an increase in temperature. In addition, the Cl  $K_\beta$  line gets significantly wider showing an increase in density, presumably as the shock wave approaches the center of the cylinder. When the shock finally reaches the center, it induces a significant increase in the continuum emission, illustrated in Fig. 4. This jump in intensity is observed between 1.5 ns and 1.55 ns, with the overall intensity increasing by a factor 1.7 over 50 ps. At this time, the foam is dense and has reached its maximum temperature. In addition, we observe a strong fluorescence emission from Ar satellites, likely coming from ions Ar<sup>9+</sup> to Ar<sup>13+</sup>, suggesting that the cones and/or the CH foil located at the end of the cylinder are getting warmer. These lines do not seem to come from the foam because they correspond to lower ionization states than one would expect considering the foam temperature (see hydrodynamics simulation later in the paper).

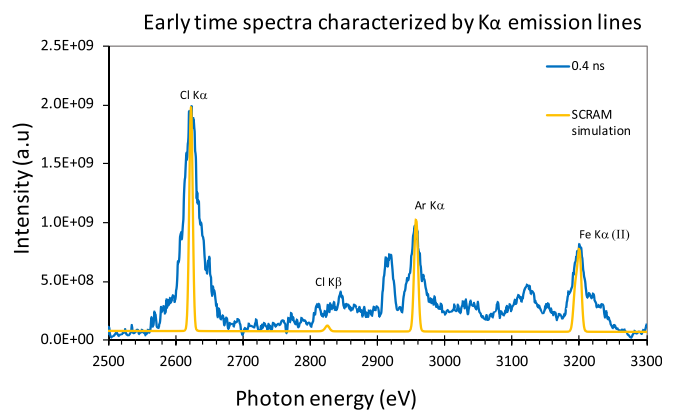
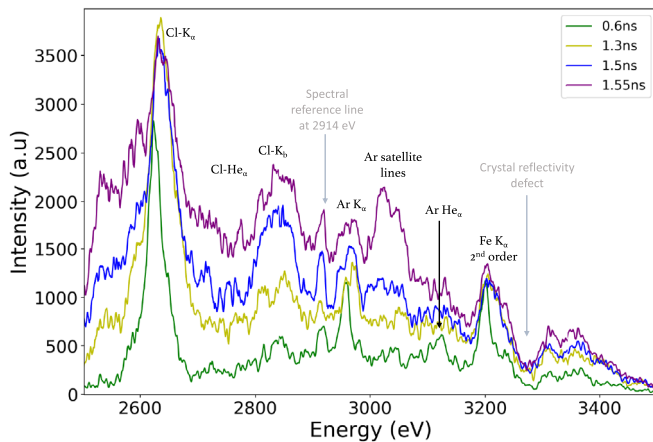


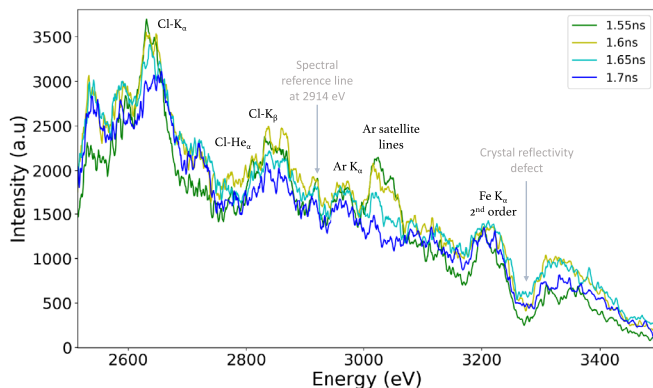
FIG. 3. Early time experimental spectrum (blue curve) compared to a simulated fluorescence spectrum (yellow curve). This comparison roughly sets the proportions of the elements in the target, which were mostly identified by XRF characterization and helps to fix the energy calibration of the spectrometer. The experimental spectrum has been normalized to the intensity values of the simulation for ease of viewing.



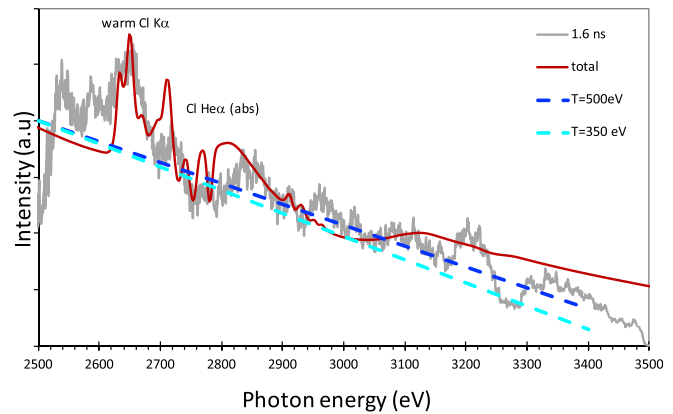
**Second phase:** The shock reaches the center of the foam

**FIG. 4.** X-ray emission spectra of the cylinder from 0.6 ns to 1.55 ns; each spectrum represents a different time. The spectra at 1.55 ns define the beginning of the stagnation period.

In the third phase, illustrated in Fig. 5, we observe a stagnation of the continuum intensity. All the spectra obtained between 1.55 ns and 1.7 ns present the same characteristics and the same continuum intensity level. This suggests that the cylinder remains hot and dense for about 150 ps. During this time, the electron temperature can be estimated using the slope of the spectra. We cannot use line ratios or shapes to infer the plasma conditions here due to extreme gradients and high line optical depths. Figure 6 shows two blue dashed curves illustrating the two limits that define reasonable fits of the continuum emission to  $\exp(-h\nu/T_e)$ , giving a range for the foam temperature between 350 eV and 500 eV. This calculation represents only a rough estimation of the foam temperature, but considering that the center of the foam is the densest part of the target at this time, it is fair to assume that the continuum emission we observed is dominantly coming from

**Third phase:** Most intense continuum emission during 150 ps

**FIG. 5.** X-ray emission spectra of the cylinder from 1.55 ns to 1.7 ns; each spectrum represents a different time. The spectra at 1.7 ns define the end of the stagnation period and the maximum compression time.

**Stagnation:** 400 eV foam (1% Cl)  
+ 300 eV CH foil

**FIG. 6.** Comparison between one experimental spectrum obtained during stagnation (gray line) and one recorded spectrum (red line) using  $T_e = 400$  eV for the compressed foam and taking into account the opacity of the target including the solid CH foil on the detection axis with its Cl impurities (see Fig. 1). The two continuum fits (dashed lines) represent the range of temperatures inferred from the continuum emission.

there. Furthermore, using the element ratio found in Fig. 3 and  $T_e = 400$  eV, SCRAM (red curve on Fig. 6) can roughly reproduce the spectrum obtained at 1.6 ns (gray curve on Fig. 6). Here, carbon emission provides the dominant contribution to the continuum. Viewing along the axis of the cylindrical stagnation column, the almost complete self-absorption of the Cl He $\alpha$  line indicates peak optical depths on the order of 1000, which are consistent with a density of 2–5 g/cm<sup>3</sup>. Additional absorption of the Cl He $\alpha$  line arises from the CH foil at the end of the cylinder, which we model as a plasma at 9 g/cm<sup>3</sup> and 300 eV (consistent with the radial compression of the endcaps to a convergence of  $\sim 3$ ). The intensity of optically thin Li-like emission at 2700 eV is overestimated by this simple picture. Some warm Cl fluorescence emission is observed at 2650 eV, which we assume to arise from cooler ( $\sim 50$  eV) plastic regions.

While the maximum temperature is reached at stagnation, the density keeps increasing until the maximum compression is reached at 1.7 ns. This time corresponds to the end of the stagnation (the very last spectrum with a high intensity in Fig. 5). After maximum compression, the plasma starts to expand and the emission intensity starts to decrease. The spectroscopic data do not allow quantitative estimates of the density evolution, but the onset of a rapid decay in the continuum intensity can be compared with the time of maximum compression in the hydrodynamics simulation.

Indeed, right after 1.7 ns, we can observe a significant drop in intensity as illustrated in Fig. 7 with the spectra from 1.8 ns to 2 ns. This is the last phase, defined by the expansion of the plasma. The implosion has finished, and the density and temperature decrease along with the spectra intensity. We do not detect lines anymore besides warm Cl K $\alpha$  emission, which is still generated by the only remaining “cold” part of the target, the cone. The continuum intensity decreases until it becomes undetectable around 2.2 ns.

The emission spectra of the cylindrical foam viewed along its axis have thus provided a detailed (if not rigorously quantitative) picture of

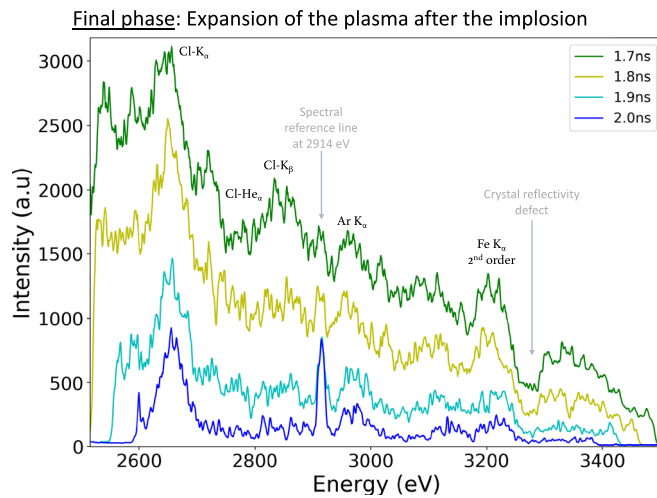


**FIG. 7.** X-ray emission spectra of the cylinder from 1.7 ns to 2.0 ns; each spectrum represents a different time.

the implosion dynamics, giving indications of distinct phases in the plasma evolution. This experimental analysis is compared to hydrodynamics simulations in the “Comparison with radiation-hydrodynamic simulation section.”

## COMPARISON WITH RADIATION-HYDRODYNAMIC SIMULATION

The emission spectroscopy data can be further interpreted alongside hydrodynamic simulations made with the radiation-magnetohydrodynamic code FLASH.<sup>38,39</sup> The code is used with PROPACEOS EOS and opacity tables to simulate the cylinder compression in 2D cylindrical coordinates and used a 3D laser ray-tracing. The simulations provided by FLASH show the overall same trend as the experimental spectroscopic data.

Figure 8 presents temperature and density calculations at 1.35 ns and 1.55 ns, which correspond to times before the maximum compression. As the spectroscopic data were showing, 1.35 ns is when the plasma ahead of the shock front is heated by radiation diffusion all the way to the center of the foam. The shock has not arrived yet as we can see with the density still close to its initial condition. Slightly later, at 1.55 ns, the shock reaches the center of the foam and the peak of temperature, which induced an increase in intensity on the experimental spectra. This time defines the beginning of the stagnation in the FLASH simulations like it was in the spectroscopic data. However, we can note that in Fig. 8, we observe a temperature of about 1.2 keV, which was not detected in the spectra. One possible explanation is that this high temperature is not dominating, being reached for only 50 ps and in the very center of the axis. Indeed, the main detectable difference expected in the spectra with such temperature would be lines from higher ionization states. In our case, it would be detecting Cl  $Ly_{\alpha}$ .

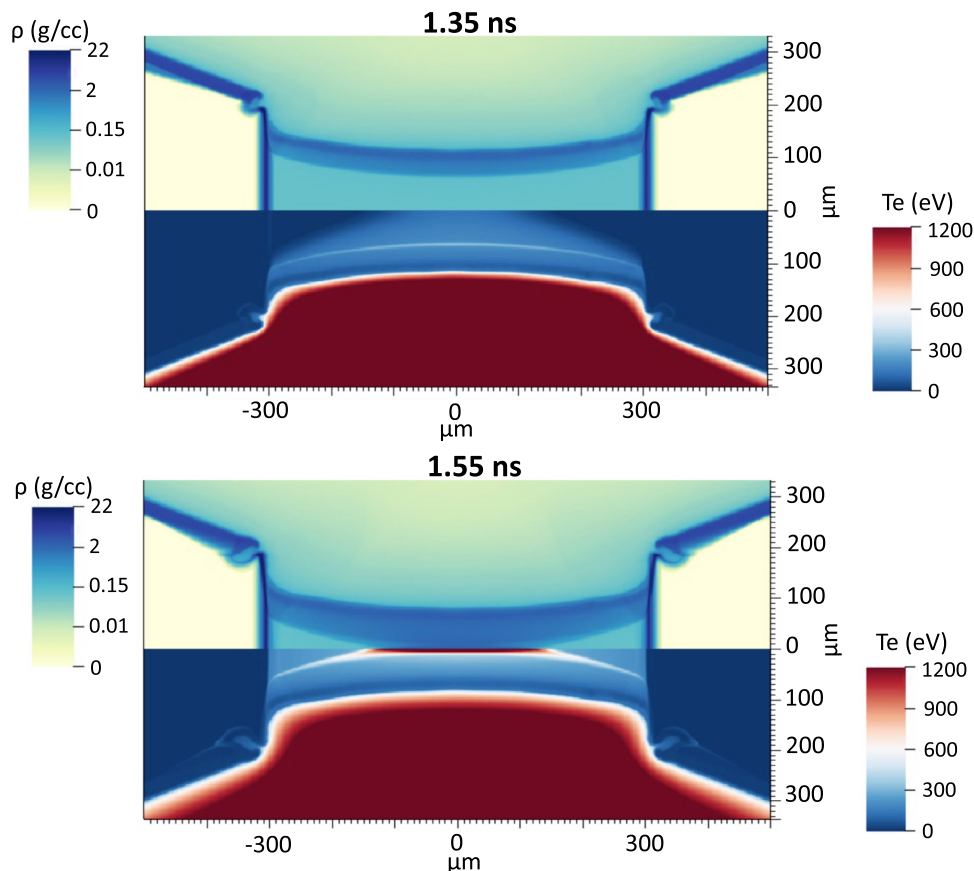


**FIG. 8.** FLASH simulations of temperature (bottom half of each picture) and density (top half of each picture) of the cylinder at 1.35 ns and 1.55 ns.

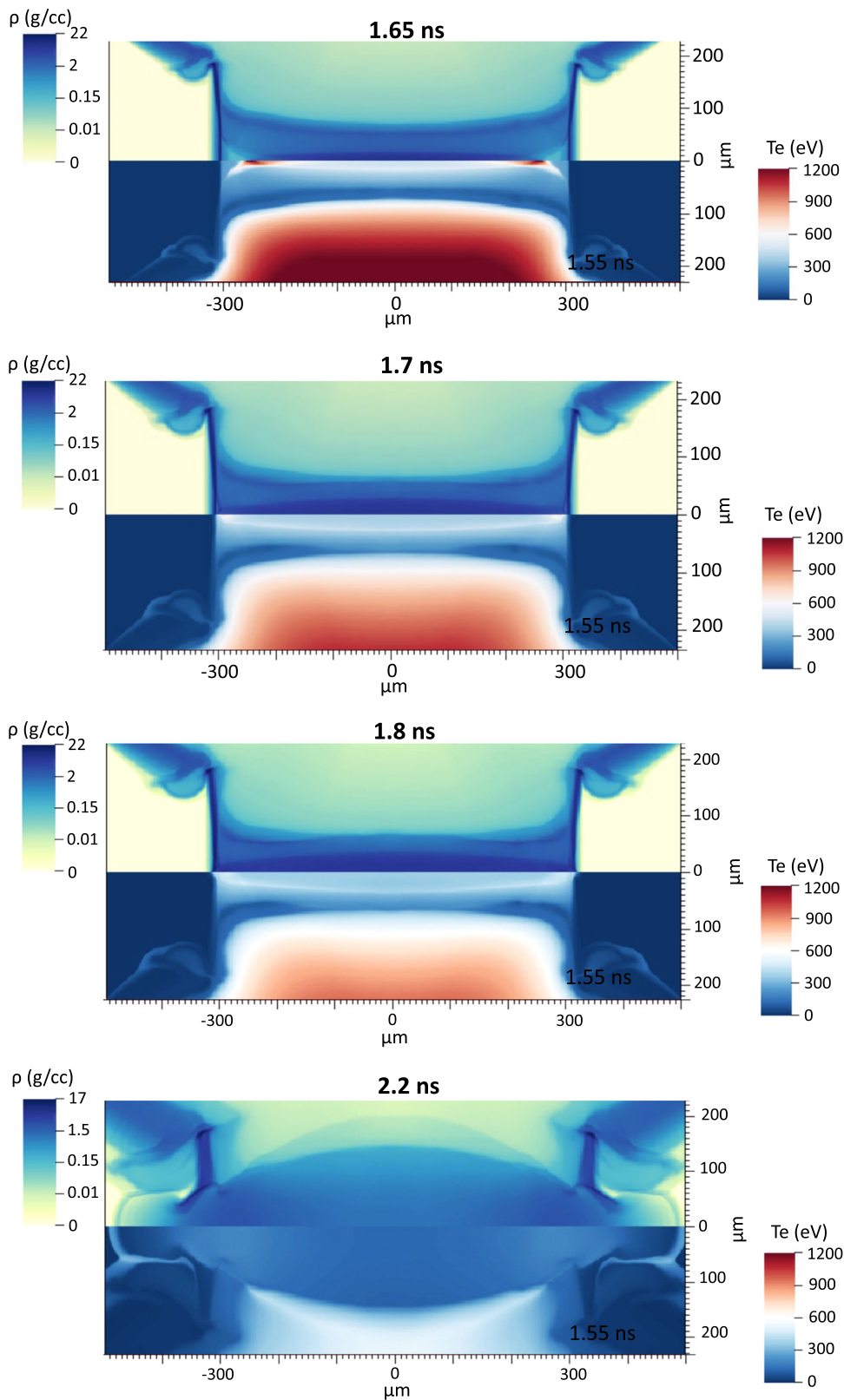


**FIG. 9.** FLASH simulations of temperature (bottom half of each picture) and density (top half of each picture) of the cylinder at 1.65 ns and 1.7 ns, the maximum compression time.

**FIG. 10.** FLASH simulations of temperature (bottom half of each picture) and density (top half of each picture) of the cylinder after the maximum compression, at 1.8 ns and 2.2 ns.

**TABLE II.** Summary of the experimental results (two shots total) compared to the FLASH simulation results. Shot 1 corresponds to the results presented in this paper.

Event	Shot 1	Shot 2	FLASH results
Jump in intensity	$1.55 \pm 0.13\text{ns}$	$1.4 \pm 0.13\text{ns}$	1.55 ns
Stagnation duration	$150 \text{ ps} \pm 30\text{ps}$	$150 \text{ ps} \pm 30\text{ps}$	150 ps
Maximum compression	$1.7 \pm 0.13\text{ns}$	$1.55 \pm 0.13\text{ns}$	1.7 ns

which, considering the small and short plasma at very high temperature, is likely not emitting enough to overcome the continuum emission. It is also possible that the simulation overestimates the temperature reached in this region of the target.

Figure 9 shows temperature and density at two later times, one during the stagnation (1.65 ns) and one at the end of it (1.7 ns). The temperature given by the calculation at 1.65 ns is about 500 eV, which is consistent with the experimental estimation (see Fig. 6) and is fairly homogeneous along the axis of the cylinder. Finally, the maximum compression is found at 1.7 ns with a density of  $9.4 \text{ g/cm}^3$  in the center of the foam. For the experimental spectra, stagnation lasts 150 ps and ends at 1.7 ns.

Figure 10 shows the simulation results for two times after the implosion, 1.8 ns and 2.2 ns. We can clearly see the expansion of the plasma starting at 1.8 ns and the temperature decreasing to finally being too cold to emit around 2.2 ns. These calculations are also consistent with the last phase of the experimental data.

Finally, another shot was taken in similar conditions (same target and same laser parameters) and presented the same spectra evolution over time as the shot data presented to this point. The same four phases could be defined but with slightly different absolute times.

Table II summarizes the results presented in this paper and the ones obtained for the second shot. Considering the errors, shot 2 shows similar results to shot 1 and to FLASH calculations. In all cases, we observe the same stagnation duration and the same evolution of the spectra. However, in view of the large time uncertainty due to trigger jitter in the diagnostic, collection of more data would be beneficial.

## CONCLUSION

X-ray emission from a laser-imploded cylindrical foam-in-shell target was spectrally and temporally resolved, allowing inference of its evolving conditions during critical times of the implosion. The data can inform future relativistic electron transport or energetic ion studies in the same imploded target or the technique could be applied to similar platforms. The experimental data obtained has been compared to rad-hydrodynamic simulations made with the code FLASH, and both show the same evolution of the compression. Four distinct phases have been defined: the ablation of the cylinder tube and the creation of a shock; the slow increase in the continuum emission created by the heat wave propagating in front of the shock; the 150 ps stagnation defined by the shock reaching the center of the cylinder and by the maximum compression; and the expansion of the plasma, which occurs after the implosion of the cylinder. In addition, we estimated the temperature inside the foam during the stagnation using the atomic physics code SCRAM that was consistent with the FLASH simulations.

We have shown that spectroscopy can be a powerful tool to obtain insight into complex plasma conditions. In future experiments,

targets with more controlled impurities (e.g., transition-metal dopants whose emission lines would remain thin and could be measured in second order) could better constrain the absolute timeline of the implosion and plasma conditions.

## ACKNOWLEDGMENTS

This material is based upon the work supported by the Department of Energy, National Nuclear Security Administration, under Award No. DE-NA0003842 and under the NLUF program with Award No. DE-FOA-0001568. The work of S.H. was supported by Sandia National Laboratories, a multi-mission laboratory managed and operated by the National Technology and Engineering Solutions of Sandia, LLC., a wholly owned subsidiary of Honeywell International, Inc., for the U.S. Department of Energy's National Nuclear Security Administration under Contract No. DE-NA-0003525. J.J.S. and D.B. were supported by the framework of the "Investments for the future" program IdEx Bordeaux LAPHIA (No. ANR-10-IDEX-03-02) and of the EUROfusion Consortium and received funding from the Euratom research and training program 2014–2018 under Grant Agreement No. 633053. The views and opinions expressed herein do not necessarily reflect those of the European Commission.

## REFERENCES

- <sup>1</sup>G. Chabrier, D. Saumon, and A. Y. Potekhin, *J. Phys. A* **39**, 4411 (2006).
- <sup>2</sup>B. A. Remington, *Plasma. Phys. Controlled Fusion* **47**, A191 (2005).
- <sup>3</sup>F. Weber, G. A. Contrera, M. G. Orsaria, W. Spinella, and O. Zubairi, *Mod. Phys. Lett. A* **29**, 1430022 (2014).
- <sup>4</sup>K. T. Lorenz, M. J. Edwards, A. F. Jankowski, S. M. Pollaine, R. F. Smith, and B. A. Remington, *High Energy Density Phys.* **2**, 113–125 (2006).
- <sup>5</sup>H. J. Lee, P. Neumayer, J. Castor, T. Döppner, R. W. Falcone, C. Fortmann, B. A. Hammel, A. L. Kritcher, O. L. Landen, R. W. Lee, D. D. Meyerhofer, D. H. Munro, R. Redmer, S. P. Regan, S. Weber, and S. H. Glenzer, *Phys. Rev. Lett.* **102**, 115001 (2009).
- <sup>6</sup>W. W. Hsing, C. W. Barnes, J. B. Beck, and N. M. Hoffman, *Phys. Plasmas* **4**, 1832 (1997).
- <sup>7</sup>K. A. Back, J. D. Bauer, J. H. Hammer, B. F. Lasinski, R. E. Turner, P. W. Rambo, O. L. Landen, L. J. Suter, M. D. Rosen, and W. W. Hsing, *Phys. Plasmas* **7**, 2126 (2000).
- <sup>8</sup>O. V. Gotchev, P. Y. Chang, J. P. Knauer, D. D. Meyerhofer, O. Polomarov, J. Freije, C. K. Li, M. J.-E. Manuel, R. D. Petrasso, J. R. Rygg, F. H. Seguin, and R. Betti, *Phys. Rev. Lett.* **103**, 215004 (2009).
- <sup>9</sup>B. A. Remington, R. P. Drake, and D. D. Ryutov, *Rev. Mod. Phys.* **78**, 755 (2006).
- <sup>10</sup>M. Brassart and J.-P. Luminet, *Astron. Astrophys.* **481**, 259–277 (2008).
- <sup>11</sup>J. H. Nuckolls, L. Wood, A. Thiessen, and G. B. Zimmerman, *Nature* **239**, 139 (1972).
- <sup>12</sup>K. A. Brueckner and S. Jorna, "Laser-driven fusion," *Rev. Mod. Phys.* **46**, 325 (1974).
- <sup>13</sup>S. A. Slutz, M. C. Herrmann, R. A. Vesey, A. B. Sefkow, D. B. Sinars, D. C. Rovang, K. J. Peterson, and M. E. Cuneo, *Phys. Plasmas* **17**, 056303 (2010).
- <sup>14</sup>M. R. Gomez, S. A. Slutz, A. B. Sefkow, D. B. Sinars, K. D. Hahn, S. B. Hansen, E. C. Harding, P. F. Knapp, P. F. Schmit, C. A. Jennings *et al.*, *Phys. Rev. Lett.* **113**, 155003 (2014).
- <sup>15</sup>A. J. Kemp, M. M. Basko, and J. Meyer-ter-Vehn, *Nucl. Fusion* **43**, 16 (2003).
- <sup>16</sup>M. Roth, T. E. Cowan, M. H. Key, S. P. Hatchett, C. Brown, W. Fountain, J. Johnson, D. M. Pennington, R. A. Snavely, S. C. Wilks, K. Yasuike, H. Ruhl, F. Pegoraro, S. V. Bulanov, E. M. Campbell, M. D. Perry, and H. Powell, *Phys. Rev. Lett.* **86**, 436 (2001).
- <sup>17</sup>M. Tabak, J. Hammer, M. E. Glinsky, W. L. Kruer, S. C. Wilks, J. Woodworth, E. M. Campbell, and M. D. Perry, *Phys. Plasmas* **1**, 1626–1634 (1994).



- <sup>18</sup>S. Wilks, W. L. Kruer, M. Tabak, and A. B. Langdon, *Phys. Rev. Lett.* **69**, 1383–1386 (1992).
- <sup>19</sup>F. N. Beg, A. R. Bell, A. E. Dangor, C. N. Danson, A. P. Fews, M. E. Glinsky, B. A. Hammel, P. Lee, P. A. Norreys, and M. Tatarakis, *Phys. Plasmas* **4**, 447 (1997).
- <sup>20</sup>K. W. D. Ledingham and W. Galster, *New J. Phys.* **12**, 045005 (2010).
- <sup>21</sup>D. J. Stark, T. Toncian, and A. V. Arefiev, *Phys. Rev. Lett.* **116**, 185003 (2016).
- <sup>22</sup>F. Perez, L. Gremillet, M. Koenig, S. D. Baton, P. Audebert, M. Chahid, C. Rousseaux, M. Drouin, E. Lefebvre, T. Vinci, J. Rassuchine, T. Cowan, S. A. Gaillard, K. A. Flippo, and R. Shepherd, *Phys. Rev. Lett.* **104**, 085001 (2010).
- <sup>23</sup>D. J. Hoarty, P. Allan, S. F. James, C. R. D. Brown, L. M. R. Hobbs, M. P. Hills, J. W. O. Harris, J. Morton, M. G. Brookes, R. Shepherd, J. Dunn, H. Chen, E. V. Marley, P. Beiersdorfer, H. K. Chung, R. W. Lee, G. Brown, and J. Emig, *Phys. Rev. Lett.* **110**, 265003 (2013).
- <sup>24</sup>R. Kodama, P. A. Norreys, K. Mima, A. E. Danger, R. G. Evans, H. Fujita, Y. Kitagawa, K. Krushelnick, T. Miyakoshi, N. Miyanaga *et al.*, *Nature* **412**, 798–802 (2001).
- <sup>25</sup>W. Theobald, A. A. Solodov, C. Stoeckl, K. S. Anderson, R. Betti, T. R. Boehly, R. S. Craxton, J. A. Delettrez, C. Dorrer, J. A. Frenje *et al.*, *Phys. Plasmas* **18**, 056305 (2011).
- <sup>26</sup>L. C. Jarrott, M. S. Wei, C. McGuffey, A. A. Solodov, W. Theobald, B. Qiao, C. Stoeckl, R. Betti, H. Chen, J. Delettrez *et al.*, *Nat. Phys.* **12**, 499–504 (2016).
- <sup>27</sup>F. Pérez, A. Debayle, J. Honrubia, M. Koenig, D. Batani, S. D. Baton, F. N. Beg, C. Benedetti, E. Brambrink, S. Chawla, F. Dorchies *et al.*, *Phys. Rev. Lett.* **107**, 065004 (2011).
- <sup>28</sup>P. Norreys, D. Batani, S. Baton, F. N. Beg, R. Kodama, P. M. Nilson, P. Patel, F. Pérez, J. J. Santos, and R. H. H. Scott, *Nucl. Fusion* **54**, 054004 (2014).
- <sup>29</sup>W. L. Kruer, *The Physics of Laser Plasma Interactions* (Taylor & Francis Inc., 2003).
- <sup>30</sup>P. Gibbon, *Short Pulse Laser Interactions with Matter: An Introduction* (Imperial College Press, 2005).
- <sup>31</sup>A. B. Sefkow, S. A. Slutz, J. M. Koning, M. M. Marinak, K. J. Peterson, D. B. Sinars, and R. A. Vesey, *Phys. Plasmas* **21**, 072711 (2014).
- <sup>32</sup>M. Millecchia, S. P. Regan, R. E. Bahr, M. Romanofsky, and C. Sorce, *Rev. Sci. Instrum.* **83**, 10E107 (2012).
- <sup>33</sup>A. A. Solodov, B. Yaakobi, D. H. Edgell, R. K. Follett, J. F. Myatt, C. Sorce, and D. H. Froula, *Phys. Plasmas* **23**, 102707 (2016).
- <sup>34</sup>B. Yaakobi, P.-Y. Chang, A. Solodov, C. Stoeckl, D. H. Edgell, R. S. Craxton, S. X. Hu, J. F. Myatt, J. F. Marshall, W. Seka, and D. H. Froula, *Phys. Plasmas* **19**, 012704 (2012).
- <sup>35</sup>D. H. Froula, B. Yaakobi, S. X. Hu, P.-Y. Chang, R. S. Craxton, D. H. Edgell, R. Follett, D. T. Michel, J. F. Myatt, W. Seka, R. W. Short, A. Solodov, and C. Stoeckl, *Phys. Rev. Lett.* **108**, 165003 (2012).
- <sup>36</sup>S. B. Hansen, J. Bauche, C. Bauhce-Arnoult, and M. F. Gu, *High Energy Density Phys.* **3**, 109–114 (2007).
- <sup>37</sup>M. F. Gu, *Can. J. Phys.* **86**, 675 (2008).
- <sup>38</sup>A. Dubey, K. Antypas, M. K. Ganapathy, L. B. Reid, K. Riley, D. Sheeler, A. Siegel, and K. Weide, *Parallel Comput.* **35**, 512 (2009).
- <sup>39</sup>B. Fryxell, K. Olson, P. Ricker, F. X. Timmes, M. Zingale, D. Q. Lamb, P. MacNeice, R. Rosner, J. W. Truran, and H. Tufo, *Astrophys. J. Suppl. Ser.* **131**, 273 (2000).